

LA-UR-17-28480

Approved for public release; distribution is unlimited.

Title: Oxide Morphology of a FeCrAl Alloy, Kanthal APMT, following Extended Aging at 300-600C

Author(s): Li, Nan
Parker, Stephen Scott
Wood, Elizabeth Sooby

Intended for: Report


Issued: 2017-09-19

Disclaimer:

Los Alamos National Laboratory, an affirmative action/equal opportunity employer, is operated by the Los Alamos National Security, LLC for the National Nuclear Security Administration of the U.S. Department of Energy under contract DE-AC52-06NA25396. By approving this article, the publisher recognizes that the U.S. Government retains nonexclusive, royalty-free license to publish or reproduce the published form of this contribution, or to allow others to do so, for U.S. Government purposes. Los Alamos National Laboratory requests that the publisher identify this article as work performed under the auspices of the U.S. Department of Energy. Los Alamos National Laboratory strongly supports academic freedom and a researcher's right to publish; as an institution, however, the Laboratory does not endorse the viewpoint of a publication or guarantee its technical correctness.

APPENDIX E

FCT DOCUMENT COVER SHEET ¹

| | |
|------------------------------------|---|
| Name/Title of | Oxide Morphology of a FeCrAl Alloys following Extended Aging |
| Deliverable/Milestone/Revision No. | M3FT-17LA020202042 |
| Work Package Title and Number | Cladding Steam Testing and Oxidation Behavior, FT-17LA02020204 |
| Work Package WBS Number | 1.02.02.02.02 |
| Responsible Work Package Manager | Andrew T. Nelson  |
| | (Name/Signature) |

Date Submitted **September 15, 2017**

| | | | | |
|--|--|--------------------------------|---|--|
| Quality Rigor Level for Deliverable/Milestone ² | <input type="checkbox"/> QRL-1 Nuclear Data | <input type="checkbox"/> QRL-2 | <input checked="" type="checkbox"/> QRL-3 | <input type="checkbox"/> QRL 4 Lab-specific |
|--|--|--------------------------------|---|--|

This deliverable was prepared in accordance with Los Alamos National Laboratory (LANL)
(Participant/National Laboratory Name)

QA program which meets the requirements of
☒ DOE Order 414.1 ☐ NQA-1 ☐ Other

This Deliverable was subjected to:

☒ Technical Review

Technical Review (TR)

Review Documentation Provided

- ☐ Signed TR Report or,
☐ Signed TR Concurrence Sheet or,
☒ Signature of TR Reviewer(s) below

Name and Signature of Reviewers

Andrew T. Nelson  9/15/2017

☐ Peer Review

Peer Review (PR)

Review Documentation Provided

- ☐ Signed PR Report or,
☐ Signed PR Concurrence Sheet or,
☐ Signature of PR Reviewer(s) below

Name and Signature of Reviewers

NOTE 1: Appendix E should be filled out and submitted with each deliverable. Or, if the PICS:NE system permits, completely enter all applicable information in the PICS:NE Deliverable Form. The requirement is to ensure that all applicable information is entered either in the PICS:NE system or by using the FCT Document Cover Sheet.

- In some cases there may be a milestone where an item is being fabricated, maintenance is being performed on a facility, or a document is being issued through a formal document control process where it specifically calls out a formal review of the document. In these cases, documentation (e.g., inspection report, maintenance request, work planning package documentation or the documented review of the issued document through the document control process) of the completion of the activity, along with the Document Cover Sheet, is sufficient to demonstrate achieving the milestone.

NOTE 2: If QRL 1, 2, or 3 is not assigned, then the QRL 4 box must be checked, and the work is understood to be performed using laboratory specific QA requirements. This includes any deliverable developed in conformance with the respective National Laboratory / Participant, DOE or NNSA-approved QA Program.

Oxide Morphology of a FeCrAl Alloy, Kanthal APMT, following Extended Aging at 300-600C

**Nuclear Technology
Research and Development**

***Prepared for
U.S. Department of Energy
Advanced Fuels Campaign
Nan Li, S. Scott Parker, and E.S. Wood
Los Alamos National Laboratory
September 15, 2017
NTRD-M3FT-17LA020202042***



DISCLAIMER

This information was prepared as an account of work sponsored by an agency of the U.S. Government. Neither the U.S. Government nor any agency thereof, nor any of their employees, makes any warranty, expressed or implied, or assumes any legal liability or responsibility for the accuracy, completeness, or usefulness, of any information, apparatus, product, or process disclosed, or represents that its use would not infringe privately owned rights. References herein to any specific commercial product, process, or service by trade name, trade mark, manufacturer, or otherwise, does not necessarily constitute or imply its endorsement, recommendation, or favoring by the U.S. Government or any agency thereof. The views and opinions of authors expressed herein do not necessarily state or reflect those of the U.S. Government or any agency thereof.

SUMMARY

Iron-chromium-aluminum (FeCrAl) alloys are of interest to the nuclear materials community due to their resistance to high temperature steam oxidation under accident conditions. The present work investigates oxide formation at temperatures relevant to light water reactor cladding operation following extended aging to assess growth kinetics, chemical composition, and microstructure of oxide formation on a commercial FeCrAl alloy, Fe-21wt.%Cr-5wt.%Al-3wt.%Mo (Kanthal APMT). Aging treatments were performed for 100-1000 hours in stagnant air at 300, 400, 500, and 600 °C, respectively. Oxide growth behavior under the investigated conditions follows a logarithmic time dependence. When the oxidization temperature is 400 °C or below, the oxide is amorphous. At 500 °C, isolated crystalline regions start to appear during short period aging time and expand with extended exposures. Crystalline α -Al₂O₃ oxide film develops at 600 °C and the correlated logarithmic rate constant decreases significantly, indicating enhanced oxidation resistance of the formed oxide film. In addition, Mo segregation at grain boundaries has been observed when the aging temperature exceeds 500 °C. The results of this study can be viewed as an upper bounding result for potential oxide coarsening during reactor operation

CONTENTS

| | |
|--|-----|
| SUMMARY | iii |
| ACRONYMS | ix |
| 1. INTRODUCTION | 1 |
| 2. EXPERIMENTAL METHODS | 3 |
| 3. RESULTS | 5 |
| 3.1 Oxidation at 300C | 5 |
| 3.2 Oxidation at 400C | 6 |
| 3.3 Oxidation at 500C | 8 |
| 3.4 Oxidation at 600C | 10 |
| 4. DISCUSSION | 13 |
| 4.1 Oxidation Kinetics | 13 |
| 4.2 Evolution of Oxide Microstructure/Morphology at Various Temperatures | 14 |
| 4.3 Comparison to the Oxidation Behavior of Similar FeCrAl Alloys | 15 |
| 5. CONCLUSIONS | 17 |
| 6. REFERENCES | 18 |

FIGURES

| | |
|---|----|
| Figure 1. APMT samples exposed to 300-600 °C for 400 hours compared to a reference, control sample. | 4 |
| Figure 2. (a) TEM micrographs of APMT alloys. In the subsurface zone (~ 750 nm beneath the surface), lamellate grains with ~ 50 nm in height and a few hundred nm in width dominate. (b) Correlated diffraction pattern with no sign of texture. | 4 |
| Figure 3. (a) Microstructure of the oxide following 100 hours at 300 °C. (b) TEM micrograph with higher magnification uncovers the thickness of oxide is about 13 nm. (c) HAADF-STEM image and (d) EDS chemical profiles across the oxide. | 5 |
| Figure 4. (a) Cross-sectional TEM micrograph with (b) higher magnification image of the oxide formed at 300 °C for 500 hours. (c) Corresponding EDS line scanning profiles across the oxide. | 6 |
| Figure 5. Cross-sectional TEM micrograph with (b) higher magnification image of the oxide formed at 400 °C for 100 hours. (c) HAADF-STEM image and (d) EDS chemical profiles across the oxide. | 7 |
| Figure 6. (a) Cross-sectional TEM micrograph with (b) higher magnification image of the oxide formed at 400 °C for 500 hours. (c) HAADF-STEM image and (d) EDS chemical profiles across the oxide. | 8 |
| Figure 7. (a) Bright field TEM and (b) HAADF-STEM micrographs of the oxide formed at 500 °C for 100 hours. (c) EDS chemical profiles across the internal grain boundary and the oxide. The oxide thickness has been measured in both (d) HAADF-STEM and (e) bright field TEM images with higher magnification. (f) HRTEM image highlighting crystalline particles with α -Al ₂ O ₃ lattice structure. | 9 |
| Figure 8. (a) Bright field TEM and (b) HRTEM micrographs of the oxide formed at 500 °C for 1000 hours. (c) HAADF-STEM image and (d) EDS chemical profiles across the internal grain boundaries and the oxide. | 10 |
| Figure 9. (a) Bright field TEM and (b) higher magnification TEM micrographs of the oxide formed at 600 °C for 100 hours. (c) HRTEM image to show the atomic configuration of the oxide film. (d) HAADF-STEM image and (e) EDS chemical profiles across the oxide. (f) HAADF-STEM image of Mo enriched particle formed internal APMT substrate and corresponding EDS analysis. | 11 |
| Figure 10. (a) Bright field TEM and (b) higher magnified TEM micrographs of the oxide formed at 600 °C for 1000 hours. (c) HAADF-STEM image and (d) EDS chemical profiles across Mo enriched particle and oxide. The chemical scan of the oxide layer is magnified in (e). | 12 |
| Figure 11. Oxide thickness as a function of aging temperatures and time. | 13 |
| Figure 12. Calculated values of the logarithmic rate constant K and x_0 | 14 |

TABLES

| | |
|---|---|
| Table 1. Alloy compositions determined by inert gas fusion technique (TC-436, Leco Corporation, St. Joseph, MI, USA), combustion infrared detection (CS-200, Leco Corporation, St. Joseph, MI, USA), and direct current plasma emission spectroscopy (SpectraSpan VI, Beckman Instruments, Andover, MA, USA)..... | 3 |
|---|---|

ACRONYMS

| | |
|--------|---|
| BWR | Boiling water reactor |
| EDM | Electrical discharge machining |
| EDS | Energy dispersion spectroscopy |
| FeCrAl | Iron-chromium-aluminum |
| FIB | Focused ion beam |
| HAADF | High angle annular dark field |
| LWR | Light water reactor |
| PWR | Pressurized water reactor |
| STEM | Scanning transmission electron microscopy |
| TEM | Transmission electron microscopy |

PROGRESS IN THE DEVELOPMENT OF FISSILE CERAMIC COMPOSITE FUELS: UO_2/UN

1. INTRODUCTION

Iron-chromium-aluminum (FeCrAl) alloys have seen limited historic use as light water reactor (LWR) applications, but modern interest in technologies capable of improving performance under accident conditions has renewed investigation of this family of alloys [1, 2]. The benefit to accident behavior accomplished by replacement of reference zirconium alloy with FeCrAl cladding is principally due to its improved resistance to high temperature steam oxidation [3]. A number of efforts are underway to better understand the behavior of FeCrAl with respect to the evolution of mechanical properties under irradiation [4], corrosion behavior [5], and other aspects relevant to fabrication, licensure, nuclear reactor service, and eventual utility deployment of this cladding concept.

One item that remains of consequence to use of FeCrAl as LWR cladding is tritium permeation. Tritium generation occurs in pressurized water reactor (PWR) coolant following neutron absorption by boron when used as a reactivity control. Use of gadolinium as a reactivity control in boiling water reactors (BWR) minimizes tritium production in the coolant. Either LWR variant will experience tritium production in the fuel itself. Potential tritium diffusion through the cladding and into the primary coolant poses an operational concern, as the increased tritium inventory in the primary coolant directly impacts the radiological consequence of coolant leaks or venting and will have implications to worker dose during operation. This is true of both PWR and BWR designs, but BWRs are more sensitive to increases in coolant radioactivity since the turbine system will come into direct contact with any coolant contaminants.

The high mobility of tritium in stainless steel cladding alloys (e.g. 304) relative to reference zirconium has been well studied, and the body of experimental data been recently expanded to include FeCrAl alloys specifically. Hu et al. demonstrated that as-fabricated FeCrAl alloys possess hydrogen permeability higher than 304 and roughly two orders of magnitude greater than conventional zirconium cladding alloys [6]. This data was then incorporated into models of tritium activity in both PWR and BWR cores confirming that use of a FeCrAl cladding alloy instead of zirconium would have an appreciable impact on coolant tritium activity for both PWR and BWR designs.

Hu et al. also propose a possible mitigation strategy to relieve this concern. A range of coating and metallurgical solutions are capable of acting as tritium barriers, but the most intriguing is alumina ($\alpha\text{-Al}_2\text{O}_3$). In addition to extremely low tritium permeability [7], Al_2O_3 could be conceivably grown on the surface of FeCrAl alloys due to the aluminum present in the alloy itself. Hu et al. demonstrated the potential of this approach by oxidizing FeCrAl in air at 1100 and 1200 °C for 1.5-2 hours resulting in Al_2O_3 layers of 0.6 to 1.9 μm thick. This thickness of oxide was then demonstrated to significantly reduce tritium permeation.

A dedicated heat treatment under such a condition would be one option to generate a tritium barrier, but such elevated temperatures may not be economical for cladding in mass production. Another possibility suggested by Hu et al. is the native coarsening of an oxide on the inside of a FeCrAl cladding. This has been hypothesized to occur through the oxygen activity that evolves during burn up for UO_2 . However, very little is known regarding the kinetics and structure of oxide formation on FeCrAl at temperatures relevant to LWR cladding operation. Literature studies have either focused on high temperature steam oxidation [3] or elevated temperature oxidation in high oxygen environments [8, 9]. These studies, while typically limited to less than 100 hours, report that $\alpha\text{-Al}_2\text{O}_3$ is not observed below 700 °C. This is significantly higher than cladding temperatures observed during normal LWR operation. If heat treatments

above 900 °C are required, significant and non-recoverable grain growth would be expected in FeCrAl alloys of interest to LWR applications [2].

The present study investigates oxide formation at temperature relevant to LWR cladding operation following extended aging to assess the effective kinetics and character of oxide coarsening on a commercial FeCrAl alloy, Fe-21wt.%Cr-5wt.%Al-3wt.%Mo (Kanthal APMT). Aging treatments were performed for 100-1000 hours in static air at 300, 400, 500, and 600 °C, respectively. These samples were then analyzed using transmission electron microscopy (TEM) to study the thickness, microstructure, and chemical composition of the surface oxide. These observations facilitate discussion of the potential for either heat treatments performed during cladding fabrication or oxide coarsening during reactor operation to mitigate tritium diffusion through FeCrAl cladding alloys.

2. EXPERIMENTAL METHODS

A 3.175 mm plate of advanced powder metallurgical, dispersion strengthened Kanthal APMT was purchased from Goodfellow Corporation (Coraopolis, Pennsylvania, USA). Chemical analysis of the as-received material was performed to independently verify the as-reported composition. Oxygen and nitrogen contents were measured using the inert gas fusion technique (TC-436, Leco Corporation, St. Joseph, MI, USA). Carbon concentration was determined using combustion infrared detection (CS-200, Leco Corporation, St. Joseph, MI, USA). All other alloy components reported in Table 1 were measured using direct current plasma emission spectroscopy (SpectraSpan VI, Beckman Instruments, Andover, MA, USA).

Table 1. Alloy compositions determined by inert gas fusion technique (TC-436, Leco Corporation, St. Joseph, MI, USA), combustion infrared detection (CS-200, Leco Corporation, St. Joseph, MI, USA), and direct current plasma emission spectroscopy (SpectraSpan VI, Beckman Instruments, Andover, MA, USA).

| Elements | Fe | Cr | Al | Mo | Y | Hf | Ti | C | N | O |
|----------------|-------|-------|------|------|------|------|------|-------|-------|-------|
| APMT (wt.%) | 70.07 | 22.20 | 4.35 | 2.90 | 0.18 | 0.14 | 0.02 | 0.036 | 0.047 | 0.060 |
| APMT (at.%) | 66.55 | 22.71 | 8.57 | 1.61 | 0.11 | 0.04 | 0.02 | 0.016 | 0.18 | 0.2 |

The stock plate was cut into 5mm x 3mm x 100mm strips by electrical discharge machining (EDM). The strips cut by EDM were subsequently sectioned into 5mm x 5mm x 3mm coupons with a diamond metal bond wafering blade in cutting lubricant on a precision low speed saw. The samples were mounted in crystal bond on a steel polishing plate and polished on all surfaces with silicon carbide grinding pads up to 1200 (P-4000) grit. Following polishing, samples were washed in acetone to remove any remaining crystal bond. Samples were then placed in methanol and loaded into an ultrasonic bath for 5 minutes. Sample mass was measured to ± 0.01 mg (Mettler Toledo, Model # XS205); sample dimension were measured to ± 0.001 mm (Mitutoyo Digimatic Indicator, Model # ID-C125EXB).

Muffle furnaces were used to expose the samples to 300, 400, 500, and 600 °C stagnant air. The set point was calibrated to $\pm 5^\circ\text{C}$ using a witness thermocouple prior to sample insertion. The samples were placed in Al_2O_3 boats. The samples were removed at temperature at 100, 200, 300, 400, and 500 hour time increments. Additional exposures for 1000 hours at 500 and 600 °C were performed using the same methodology. The samples were weighed prior to testing and following removal from the furnaces. While no mass gain was measured beyond the error of the balance, each sample appeared to have grown an oxide film, even at the 100 hours mark. Fig. 1 illustrates the different appearance of the samples with increasing temperature.

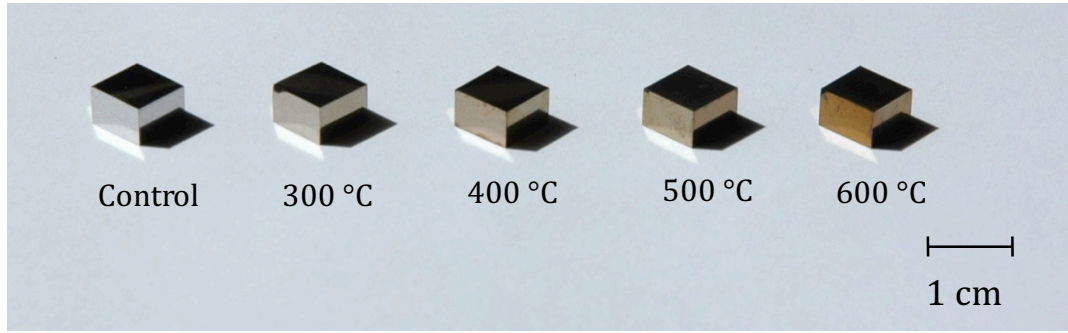


Figure 1. APMT samples exposed to 300-600 °C for 400 hours compared to a reference, control sample.

TEM was utilized to study representative foils taken from the cross section of the oxide layer and underlying substrate. Sample preparation was performed with a dual Focused Ion Beam (FIB) (Helios Nanolab DualBeam, FEI). Foil location was taken from the surface of the APMT sample away from any edge or vertex of the sample. The final cleaning step was performed with beam current of 50 pA and a voltage of 10 keV, in which FIB induced damage is minimized. The oxide microstructure, thickness and the elemental distribution as a function of depth across the oxide and in the subsurface zone was measured in an FEI Tecnai F30 field emission TEM equipped with a PHENIX energy dispersive X-ray spectrometer (EDX or EDS) detector. The combined error of EDS analysis is limited to $\pm 2\%$. The typical microstructure of the studied APMT alloy with correlated diffraction pattern is present in Fig. 2. The adjacent substrate has recrystallized to a depth of ~ 750 nm, which is likely due to alloy surface preparation as reported previously [5].

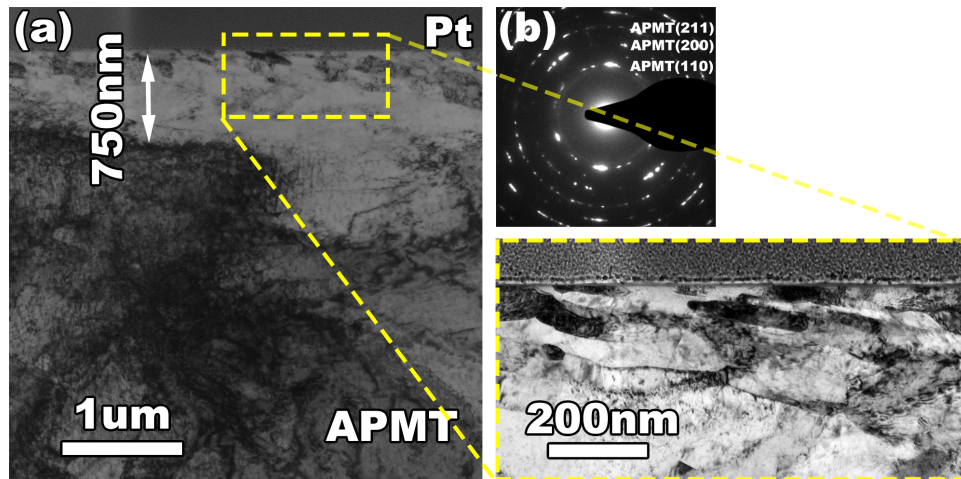


Figure 2. (a) TEM micrographs of APMT alloys. In the subsurface zone (~ 750 nm beneath the surface), lamellate grains with ~ 50 nm in height and a few hundred nm in width dominate. (b) Correlated diffraction pattern with no sign of texture.

3. RESULTS

3.1 Oxidation at 300C

Fig. 3a presents the microstructure of the oxide film and underlying APMT substrate. The top layer is platinum (Pt) deposited during TEM sample preparation. A higher magnification micrograph is present in Fig. 3b and the thickness of the oxide is 13.0 ± 0.5 nm. The oxide formed at 300 °C is amorphous without any sign of crystallinity. Fig. 3c presents the high angle annular dark field scanning TEM (HAADF-STEM) image, which is highly sensitive to atomic-number contrast. The thickness measured from the STEM image agrees well with that measured from the bright field TEM micrograph. Multiple EDS lines were performed across the oxide film to ensure repeatability, and the correlated chemical elemental profiles are displayed in Fig. 3d. The oxide layer is mainly composed of Cr and O with close 1:1 stoichiometry. At the APMT/oxide interface, slight Fe segregation and Cr depletion is detected. Note that the Pt is deposited during TEM sample preparation process. It has no relationship with the oxidation behavior of APMT alloys. Thus the corresponding chemical profile is not presented in the subsequent EDS analysis.

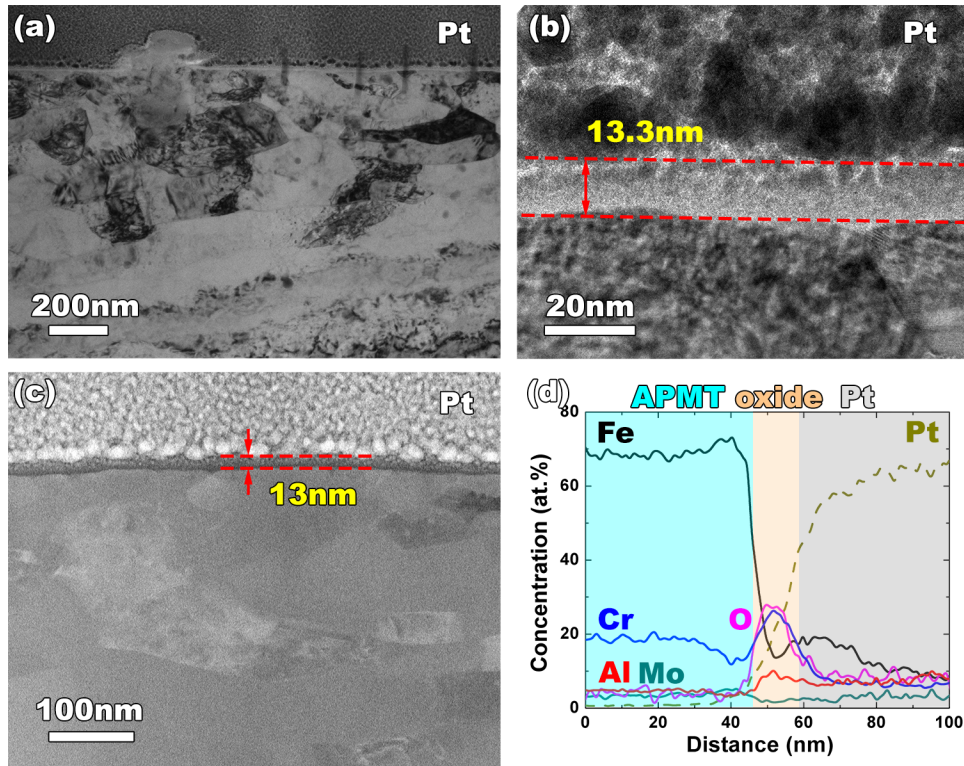


Figure 3. (a) Microstructure of the oxide following 100 hours at 300 °C. (b) TEM micrograph with higher magnification uncovers the thickness of oxide is about 13 nm. (c) HAADF-STEM image and (d) EDS chemical profiles across the oxide.

A cross-sectional TEM micrograph and corresponding chemical analysis of the oxide developing at 300 °C aging for 500 hours is shown in Fig. 4. The microstructure of APMT substrate does not change significantly by compared to the 100 hour anneal. The correlated oxide layer still remains amorphous, and

the thickness slightly increases to about 14.4 ± 0.4 nm (as labeled in Fig. 4b). EDS line scanning (in Fig. 4c) indicates that under current oxidation condition, the concentration of Fe and Cr in the oxide are comparable and amorphous FeCr oxide is the major product. It is noted that limited O signal has been detected in the Pt layer. This may be due to the absorption of oxygen atoms at TEM foil surface.

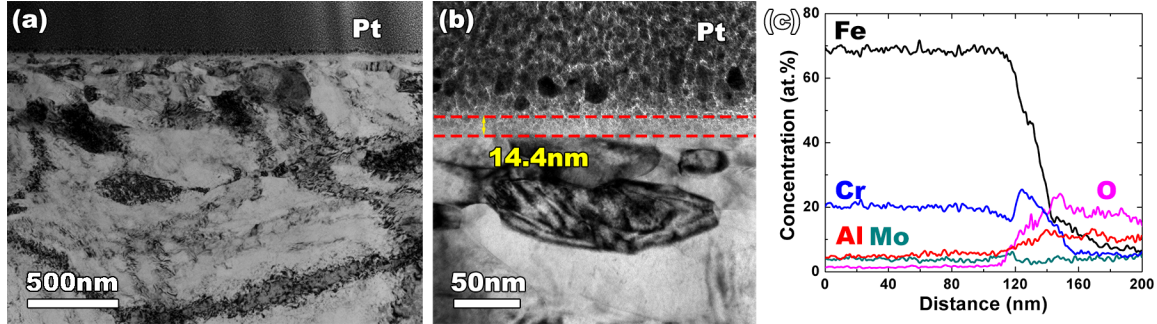


Figure 4. (a) Cross-sectional TEM micrograph with (b) higher magnification image of the oxide formed at 300 °C for 500 hours. (c) Corresponding EDS line scanning profiles across the oxide.

3.2 Oxidation at 400C

Oxidation behavior of APMT at 400 °C for 100 hours is similar to that at 300 °C. Fig. 5a is a representative bright field TEM image, and Fig. 5b is taken at higher magnification. The oxide film thickness is 16.3 ± 0.7 nm. The HRTEM image (not shown here) again found that the oxide is fully amorphous. The HAADF-STEM image is presented in Fig. 5c and reveals similar morphology compared to the 300 °C oxide. Multiple EDS line scans were made across the oxide layer at different locations. The corresponding chemical element profiles are plotted in Fig. 5d. The peaks of Cr and O concentrations are clearly observed in the oxide, indicating formation of Cr oxide. Fe concentration decreases from the substrate APMT side to the oxide, and a small Fe peak appears near the oxide surface, indicating Fe enrichment at the oxide surface.

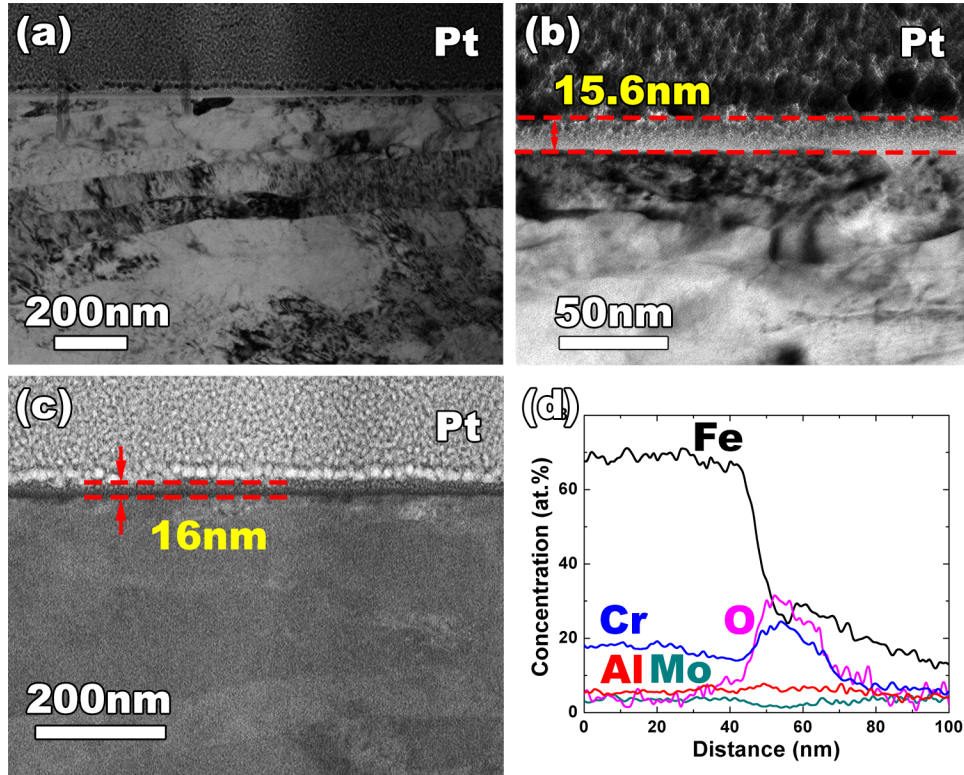


Figure 5. Cross-sectional TEM micrograph with (b) higher magnification image of the oxide formed at 400 °C for 100 hours. (c) HAADF-STEM image and (d) EDS chemical profiles across the oxide.

At 400 °C, when the exposure time has been increased to 500 hours, the microstructure of APMT adjoining to the oxide changes; nanoscale voids with a diameter of approximately 10 - 30 nm are observed beneath the oxide layer. Fig. 6a shows the microstructure of substrate APMT and the oxide, and Fig. 6b is the magnified image of the region labeled by the blue dashed box in Fig. 6a. Blue arrows label the position of voids. The oxide film still remains amorphous, and the thickness increases to 17.8 ± 0.6 nm. In HAADF-STEM image, the specimen regions containing voids tend to scatter fewer electrons in comparison to fully compacted part, and thus are illuminated to be darker. In Fig. 6c, a distribution of dark dots, correlated to the voids, are found to adhere to APMT/oxide interfaces at the APMT side. Corresponding EDS line scanning profiles are configured in Fig. 6d. The Cr and Fe distribution in oxide is not uniform. A peak of Cr and a peak of Fe are present at the inner and outer parts of the oxide, respectively. Aluminum enrichment in the oxide region is negligible at this condition.

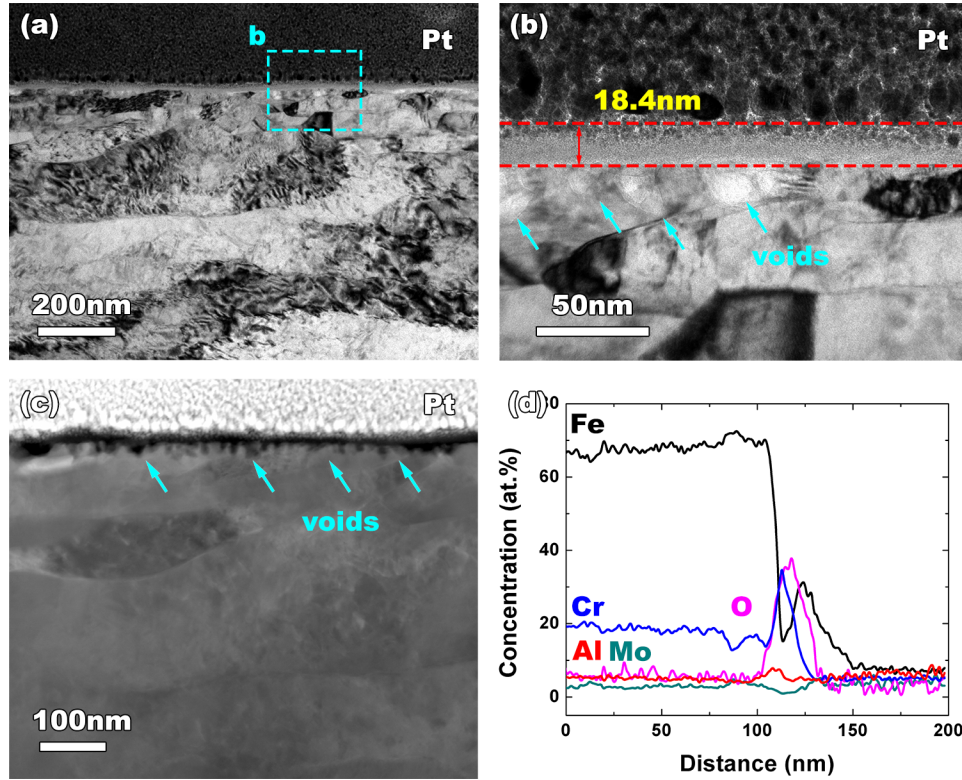


Figure 6. (a) Cross-sectional TEM micrograph with (b) higher magnification image of the oxide formed at 400 °C for 500 hours. (c) HAADF-STEM image and (d) EDS chemical profiles across the oxide.

3.3 Oxidation at 500C

When the oxidation temperature is increased to 500 °C, Mo segregation at grain boundaries is observed. In Fig. 7a, as labeled by blue arrows, the contrast at grain boundaries slightly changes, and the boundaries are thicker, but less defined, than comparable images collected at lower temperatures. The same observation is apparent in the HAADF-STEM image (in Fig. 7b). The correlated EDS line scan across the internal grain boundaries exhibits significant Mo enrichment and Fe depletion at the boundary. In addition, the chemical composition of the oxide changes in comparison to lower temperatures. An Al EDS peak is clearly present within the oxide and is accompanied by an increase in the concentration of oxygen. Fig. 7d and 7e are magnified HAADF-STEM and bright field TEM images, respectively. The thickness of oxide layer is 29.7 ± 0.3 nm. Fig. 7f is the HRTEM image. Although most of the oxide is amorphous, sparsely distributed crystalline particles with α -Al₂O₃ lattice structure are detected at APMT/oxide interface.

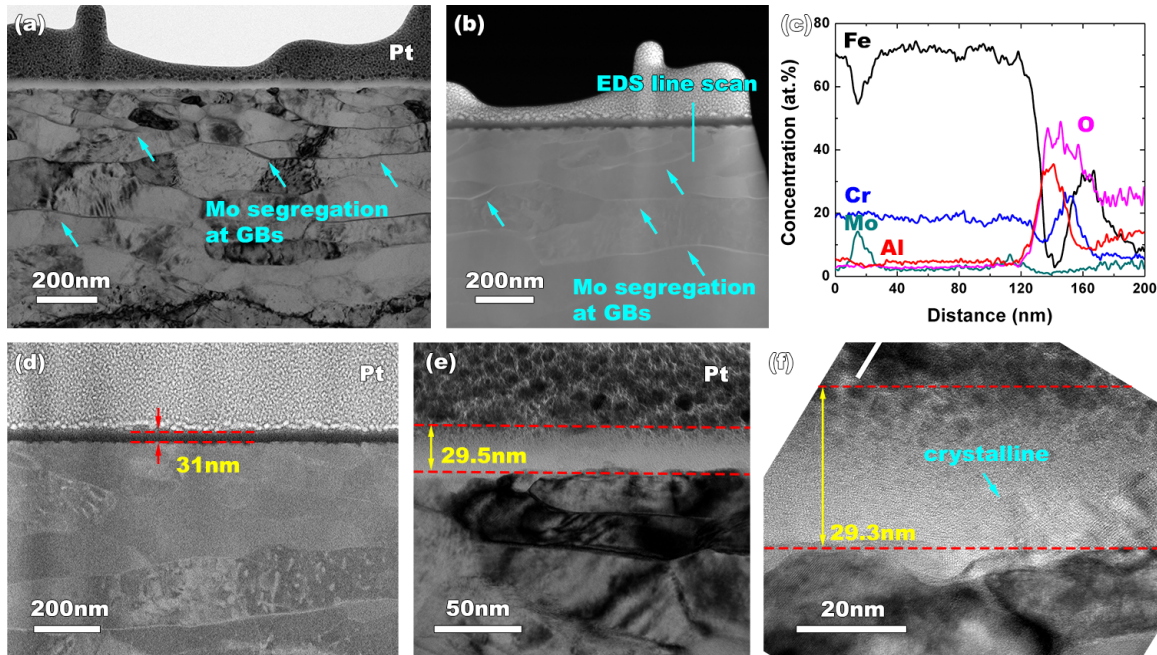


Figure 7. (a) Bright field TEM and (b) HAADF-STEM micrographs of the oxide formed at 500 °C for 100 hours. (c) EDS chemical profiles across the internal grain boundary and the oxide. The oxide thickness has been measured in both (d) HAADF-STEM and (e) bright field TEM images with higher magnification. (f) HRTEM image highlighting crystalline particles with α - Al_2O_3 lattice structure.

When the oxidation time is extended to 1000 hours, voids appear in oxides. Fig. 8a presents the typical microstructure of the oxide at 500 °C aging for 1000 hours. Voids with a variety of diameters (10 - 40 nm) are probed inside the oxide film. It is noted that the location is different from former scenario of 400 °C oxidation, which indicate a different growth mechanism. The oxide thickness is 31.0 ± 1.6 nm. In comparison to the microstructure of the oxide formed during short aging time, a greater percentage of the oxide is crystalline in the 1000 hour anneal. As shown in Fig. 8b, most of oxide becomes crystalline α - Al_2O_3 . Fig. 8c is the HAADF-STEM image and Fig. 8d is the corresponding EDS line scan across multiple grain boundaries and the oxide. Correlated with Mo enrichment and Fe depletion at grain boundaries, Cr segregation is observed as well. The chemical analysis uncovers the multilayered structure of the oxide: Al concentration peak is present at the inner boundary, while Cr and Fe peaks in the outer region of the oxide.

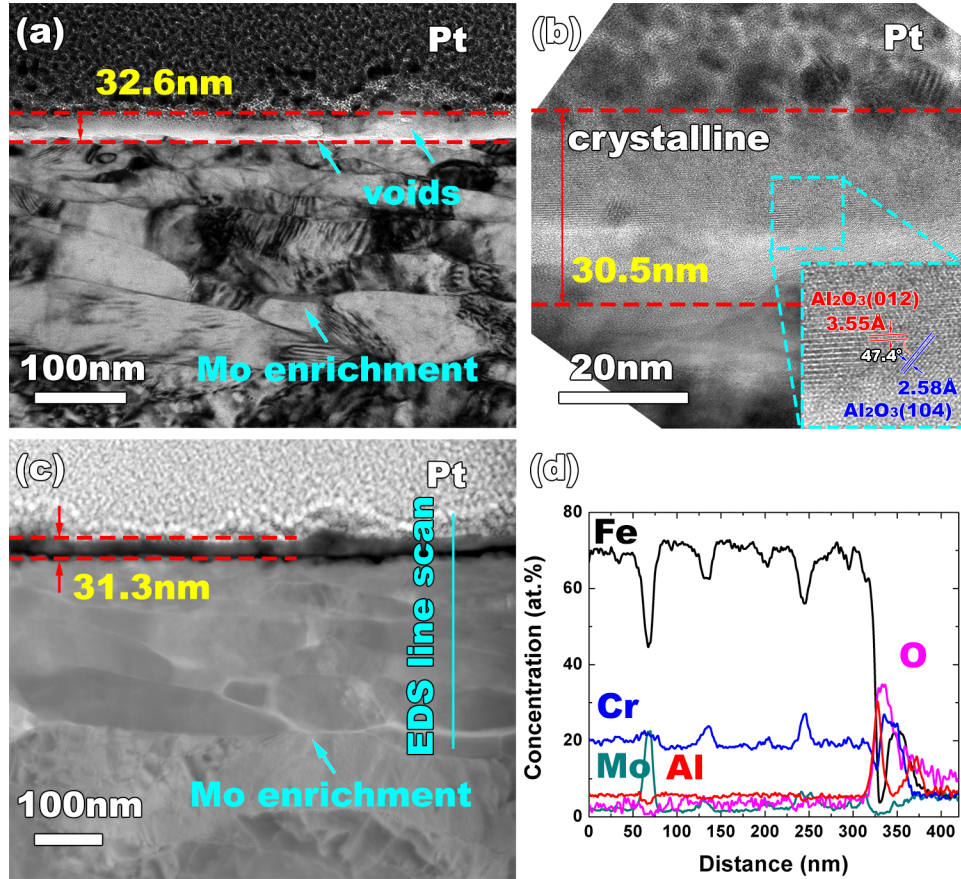


Figure 8. (a) Bright field TEM and (b) HRTEM micrographs of the oxide formed at 500 °C for 1000 hours. (c) HAADF-STEM image and (d) EDS chemical profiles across the internal grain boundaries and the oxide.

3.4 Oxidation at 600C

Fig. 9a is the microstructure of APMT oxidized at 600 °C for 100 hours. The thickness of oxide is measured to be 34.3 ± 1.3 nm. Inside APMT substrate, except for Mo segregation at grain boundaries, sparsely dispersed nanoscale precipitates with a diameter of 100 to 300 nm start to form. As shown in Fig. 9f, these particles are Mo enriched but Fe depleted. In comparison to matrix composition, Cr is slightly depleted in these precipitates. The lattice structure of the surface oxide is shown in Fig. 9c. The oxide is identified to be $\alpha\text{-Al}_2\text{O}_3$. The scenario of Mo segregation at grain boundaries can clearly be seen in the HAADF-STEM image with dramatically different contrast at boundary regions (Fig. 9d). The chemical line scan of the oxide is shown in Fig. 9e. In contrast to the previous cases, the concentration of O in oxide increases significantly. The multilayered structure oxide forms with Al enrichment at the inner and Cr, Fe enrichment in the outer region of the oxide.

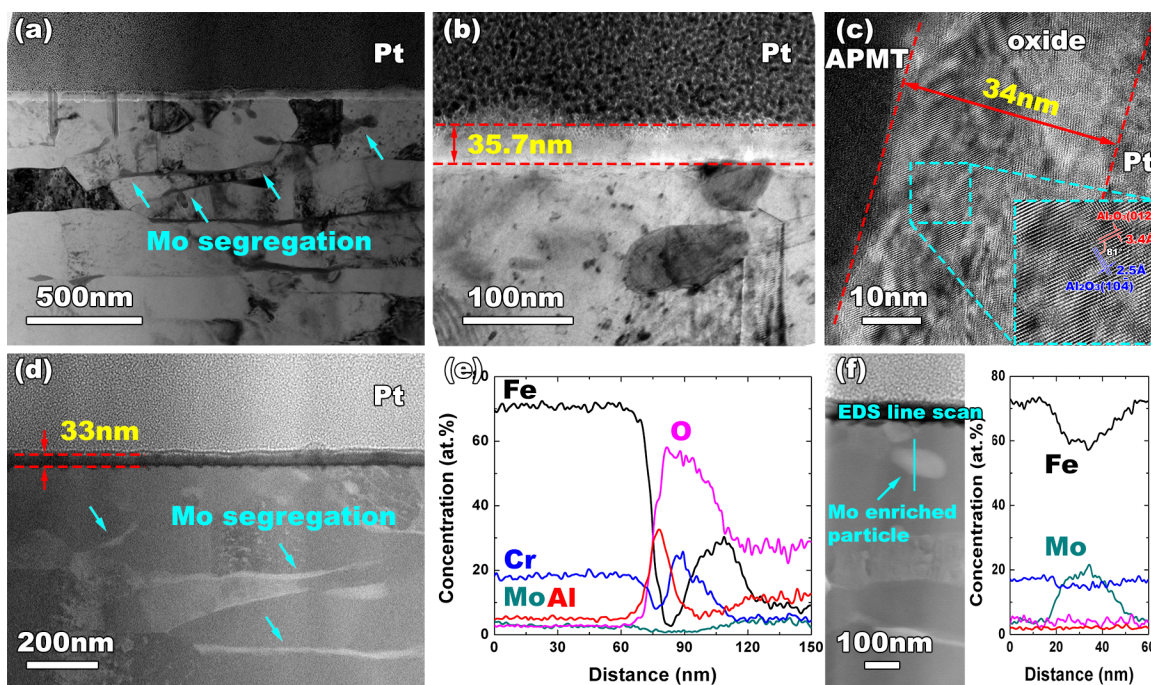


Figure 9. (a) Bright field TEM and (b) higher magnification TEM micrographs of the oxide formed at 600 °C for 100 hours. (c) HRTEM image to show the atomic configuration of the oxide film. (d) HAADF-STEM image and (e) EDS chemical profiles across the oxide. (f) HAADF-STEM image of Mo enriched particle formed internal APMT substrate and corresponding EDS analysis.

When the aging time is extended to 1000 hours, the microstructure of both APMT substrate and the surface oxide layer change significantly. Fig. 10a is the bright field TEM image and Fig. 10b is a more highly magnified image of the oxide. In contrast to the oxide film formed at 100 hours, a high density of voids are captured at oxide/APMT interface. The thickness of the oxide increases to 48.5 ± 1.4 nm. Fig. 10c is the HAADF-STEM image. Both Mo segregation at grain boundaries and the formation of Mo enriched precipitates are labeled. The correlated chemical profiles across the precipitates and oxide are present in Fig. 10d. It is noted that these precipitates are Mo enriched, but Fe and Cr are depleted in comparison to matrix composition. The chemical scan of the oxide layer is magnified in Fig. 10e, and multilayered configuration is established as well: Al is enriched in the inner region and Cr and Fe are enriched at the outer region of the oxide.

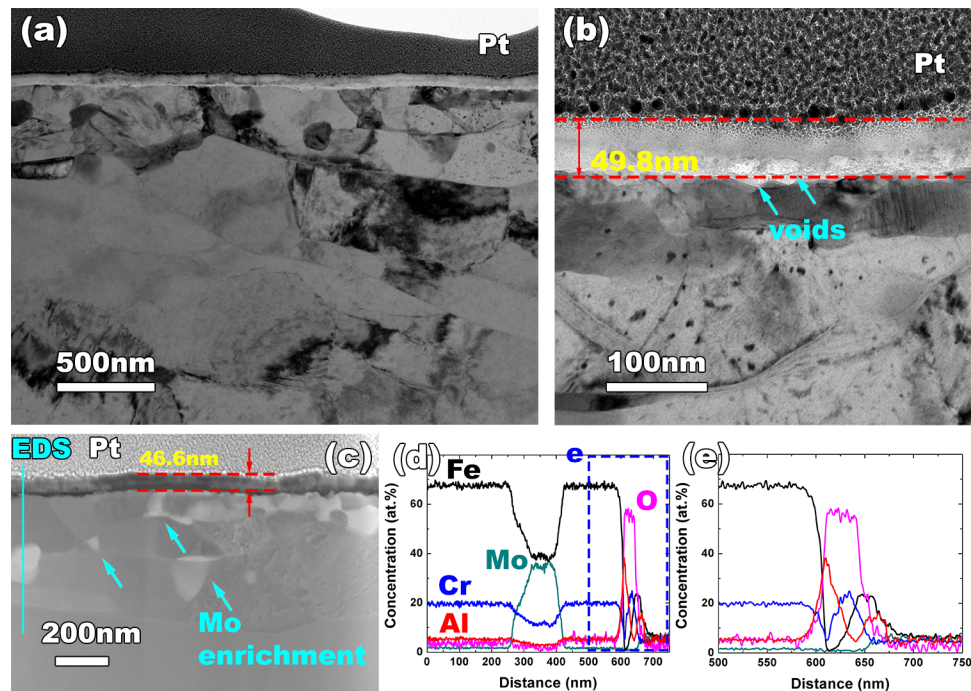


Figure 10. (a) Bright field TEM and (b) higher magnified TEM micrographs of the oxide formed at 600 °C for 1000 hours. (c) HAADF-STEM image and (d) EDS chemical profiles across Mo enriched particle and oxide. The chemical scan of the oxide layer is magnified in (e).

4. DISCUSSION

4.1 Oxidation Kinetics

Fig. 11 shows oxide thickness growth curves for APMT in stagnant air at 300 - 600 °C. The oxidation rate is rapid initially but slows due to the formation of protective oxide scales. Different from the former high temperature studies performed in dry O₂, here the oxidation kinetics follows logarithmic time dependence. It is noted that the minimum oxidation time in our experimental setup is 100 hours, which is far beyond the initial oxide growth stage and exposure times typical of higher temperature investigations. However, minimal oxide coarsening is observed in the 300 and 400 °C anneals regardless of exposure time. It is not until the temperature reaches 500 °C that oxide coarsening is observed to affect the native oxide thickness.

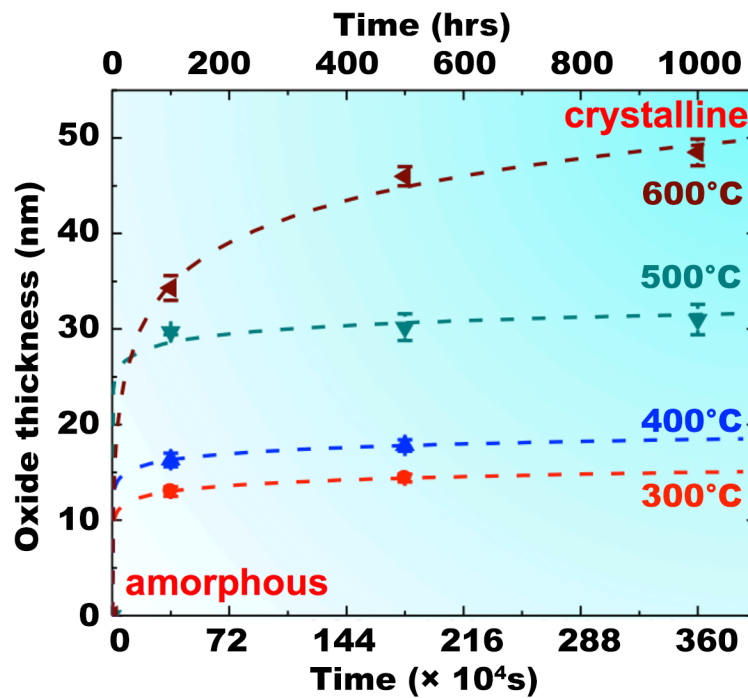


Figure 11. Oxide thickness as a function of aging temperatures and time.

The logarithmic rate model has been initiated by Mott[10, 11], and further elaborated by various groups with different assumptions[12-16]. Generally, the work required to bring an electron from the metal into the oxide (ϕ) is high for the oxide films formed on Al or Cr. That is to say, it is at least greater than the work required to bring a positive ion from the metal to an interstitial position in the oxide. We thus expect the growth of oxide films on APMT in current conditions to follow Mott's earlier model, in which electron tunneling through the oxide film is the rate determining step. The logarithmic rate equation for the growth of oxide films can be expressed by

$$x = x_0 \ln\left(\frac{Kt}{x_0} + \text{const.}\right),$$

where x is oxide thickness, t is the time, K and x_0 are constants.

The logarithmic law of growth gives a practically negligible rate of coarsening above a certain thickness. To some extent, the constant x_0 is correlated to the magnitude of the obtainable maximum oxide thickness under measured environments. The larger x_0 is, the larger the magnitude of the obtainable maximum oxide thickness. On the other hand, K is the logarithmic rate constant, correlating to oxide growth rate. The magnitude of K may be considered as an indication of how good the oxidation resistance is for the formed oxide film. The calculated constant x_0 and K values on the logarithmic growth model in our studies are shown in Fig. 12. When the temperature increases to 600 °C, the obtainable maximum oxide thickness increases accordingly. It is noted that the corresponding oxidation resistance is enhanced significantly, indicating that the oxide formed at 600 °C is extraordinarily different from the film formed at lower temperatures. This is consistent with our TEM observations.

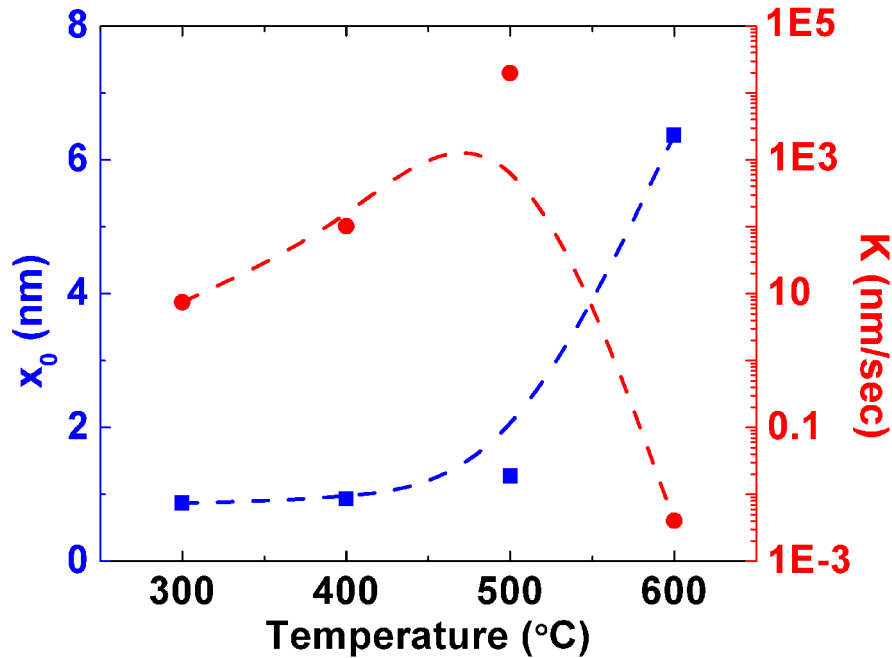


Figure 12. Calculated values of the logarithmic rate constant K and x_0 .

4.2 Evolution of Oxide Microstructure/Morphology at Various Temperatures

With extended aging time and elevated aging temperatures, the surface oxide morphology changes from amorphous to crystalline. Specifically, under conditions of the present investigation, amorphous oxide develops at 400 °C or below, while crystalline oxide films have formed at 600 °C. 500 °C seems to fall in the transition temperature region, across which the microstructure of oxide changes. At 500 °C, isolated crystalline regions have been detected during short aging period, but continuous crystalline films are observed following extended aging.

Correlated with the evolution of oxide microstructure, the chemical composition changes as well. When the aging temperature is low (400 °C or below), the concentration of Cr and O are comparable in oxide with negligible amount of Al. Only when the temperature increases to 500 °C or above does Al concentration peak start to appear, and it is always located at inner side of the oxide. Meanwhile, the oxygen

concentration has increased slightly at 500 °C but significantly at 600 °C, which is correlated to the formation of crystalline α -Al₂O₃. Josefsson et al. reported a marked decrease in the concentration of Fe and Cr within the oxide with increasing temperature when FeCrAl alloys are oxidized in dry O₂. However, in this work appreciable amounts of Cr and Fe are still present in oxide at 600 °C, with correlated concentration peaks at the outer region of the oxide. At 500 °C or above, Mo segregation at alloy grain boundaries is also observed. When the temperature increases to 600 °C, Mo enriched precipitates are observed in the vicinity of grain boundaries. As the present investigation characterized only a single alloy composition, no conclusions are possible regarding the effect of Mo segregation on oxidation behavior. It is also hypothesized that the segregation occurs as a result of thermal annealing alone rather than any impact of oxidation, but this was not investigated further. It is possible that the mechanical properties of APMT may evolve following the segregation of Mo to grain boundaries. Interpretation of mechanical property measurements of FeCrAl compositions irradiated for extended times at temperatures above 500 °C may therefore benefit from further investigation of microstructural evolution following thermal aging in this family of alloys.

4.3 Comparison to the Oxidation Behavior of Similar FeCrAl Alloys

FeCrAl alloys are known for their superior oxidation resistance up to very high temperatures. In recent years, the oxidation behavior of FeCrAl alloys with various chemical compositions under different corrosion environments has been explored. The four key observations and trends are generalized as follows.

- (i) Al and Cr concentrations are critical. It is generally accepted that Cr must be present in order to promote the growth of α -Al₂O₃. In addition, a close relationship between Al concentration and oxide film structure has been reported. The study of Fe-Cr(10 wt.%)-Al(2~8 wt.%) alloys in pure oxygen at 1 atm. pressure over the temperature range 950 – 1050 °C revealed that the lower-aluminum alloys (2–4 wt.% Al) yielded Fe-rich oxide films, whereas those containing Al in the range of 6–8 wt.% formed α -Al₂O₃ [17].
- (ii) High temperature (especially > 1000 °C) oxidation conditions assist the formation of α -Al₂O₃ [2, 3, 18-28]. Even when the temperature has increased to 1475 °C, a protective α -Al₂O₃ film can still be formed on APMT (Fe-22 wt.%Cr-5 wt.%Al-3 wt.%Mo) for a short period exposure time in both steam and dry air [29]. Below 1000°C, metastable γ -Al₂O₃ and/or θ -Al₂O₃ are also observed [30-32].
- (iii) Oxide growth rate is temperature dependent: Air oxidation studies of FeCr(19~21 wt.%)Al(5~6 wt.%) alloys at temperatures in the range of 1000 to 1300 °C found that a cubic or near-cubic time dependence of the oxidation kinetics prevails [33]. In the range of 900~1050 °C, the rate of oxidation was nearly constant [34], and a parabolic rate law developed for the temperature range 700~900°C.
- (iv) Slight amounts of reactive elements, especially Y, significantly change the oxide film growth rate, microstructure and correlated adhesion to the substrate [35-40]. However, the investigation of varying alloy compositions is not the focus of this study.

While the above conclusions are established for oxidation of FeCrAl alloys at elevated temperatures (> 800°C), investigations of intermediate temperature oxidation behavior of FeCrAl alloys over longer time periods are limited. Recent *in situ* synchrotron glancing incidence x-ray diffraction studies uncovered that at 283-417 °C and 0.158 Pa O₂ partial pressure (approximately 1 part per million O₂), Fe₃O₄ oxide were

developed across the entire Fe-Cr(10~45 at.%)–Al(0~5 at.%) composition region [21]. In addition, Fe_2O_3 peaks were also observed at 353 °C. During hydrogen water chemistry tests (i.e. autoclave testing) at 290–330 °C, bilayer structured oxide is formed on FeCr(10–15 wt.%)Al(3–5 wt.%) alloy surfaces; a Cr-rich spinel is developed at the internal region and Fe-rich spinel crystals were formed on its outer surface [5]. The oxide of Fe-21wt.%Cr-5wt.%Al formed at 500 °C in dry O_2 contains comparable amount of Fe and Al, with relatively high concentrations of Cr [9]. The concentration of Fe and Cr in the oxide decreases with temperature. The formation of $\alpha\text{-Al}_2\text{O}_3$ has not been previously observed below 700 °C. Contrary to what has previously been reported, our investigation found that a continuous crystalline $\alpha\text{-Al}_2\text{O}_3$ can be developed at temperatures as low as 600 °C with evidence of isolated crystalline structure at 500 °C.

As described at very beginning of this paper, the formation of $\alpha\text{-Al}_2\text{O}_3$ can potentially be used as a tritium barrier. Hu et al. demonstrated the viability of 0.6 μm and thicker oxide layers in limiting tritium permeation [6]. According to the logarithmic growth model discussed in 4.1, in 600 °C stagnant air, 10^{36} years would be required to coarsen $\alpha\text{-Al}_2\text{O}_3$ to 0.6 μm . If this thickness is the minimum needed to mitigate tritium diffusion, aging at this temperature under any oxygen activity either in or out-of-pile will be ineffective.

5. CONCLUSIONS

In this work, aging treatments were performed on a commercial FeCrAl alloy, Kanthal APMT, for 100-1000 hours in stagnant air at 300, 400, 500, and 600 °C. The oxide growth behavior under the investigated conditions follows a logarithmic time dependence. The oxide microstructure changes from amorphous to crystalline α -Al₂O₃ with increasing aging temperatures. Mo segregation at grain boundaries has been observed when the aging temperature is 500 °C or above. The microstructure and growth kinetics of oxide formation on FeCrAl at temperatures relevant to LWR cladding operation as studied here suggest that α -Al₂O₃ coarsening to the extent required to limit tritium diffusion is unlikely unless higher temperatures are employed.

6. REFERENCES

- [1] K.A. Terrani, S.J. Zinkle, L.L. Snead. Advanced oxidation-resistant iron-based alloys for LWR fuel cladding, *Journal of Nuclear Materials* 448 (2014):420-435.
- [2] Y. Yamamoto, B.A. Pint, K.A. Terrani, K.G. Field, Y. Yang, L.L. Snead. Development and property evaluation of nuclear grade wrought FeCrAl fuel cladding for light water reactors, *J. Nucl. Mater.* 467 (2015):703-716.
- [3] B.A. Pint, K.A. Terrani, M.P. Brady, T. Cheng, J.R. Keiser. High temperature oxidation of fuel cladding candidate materials in steam-hydrogen environments, *Journal of Nuclear Materials* 440 (2013):420-427.
- [4] K.G. Field, S.A. Briggs, K. Sridharan, R.H. Howard, Y. Yamamoto. Mechanical properties of neutron-irradiated model and commercial FeCrAl alloys, *Journal of Nuclear Materials* 489 (2017):118-128.
- [5] K.A. Terrani, B.A. Pint, Y.J. Kim, K.A. Unocic, Y. Yang, C.M. Silva, H.M. Meyer, R.B. Rebak. Uniform corrosion of FeCrAl alloys in LWR coolant environments, *Journal of Nuclear Materials* 479 (2016):36-47.
- [6] X. Hu, K.A. Terrani, B.D. Wirth, L.L. Snead. Hydrogen permeation in FeCrAl alloys for LWR cladding application, *Journal of Nuclear Materials* 461 (2015):282-291.
- [7] R.A. Causey, R.A. Karnesky, C. San Marchi. 4.16 - Tritium Barriers and Tritium Diffusion in Fusion Reactors A2 - Konings, Rudy J.M. *Comprehensive Nuclear Materials*. Oxford: Elsevier, 2012. p.511-549.
- [8] S.E. Sadique, A.H. Mollah, M.S. Islam, M.M. Ali, M.H.H. Megat, S. Basri. High-Temperature Oxidation Behavior of Iron–Chromium–Aluminum Alloys, *Oxidation of Metals* 54 (2000):385-400.
- [9] H. Josefsson, F. Liu, J.E. Svensson, M. Halvarsson, L.G. Johansson. Oxidation of FeCrAl alloys at 500–900 C in dry O₂, *Materials and Corrosion* 56 (2005):801-805.
- [10] N. Mott. A theory of the formation of protective oxide films on metals, *Transactions of the faraday Society* 35 (1939):1175-1177.
- [11] N. Mott. The theory of the formation of protective oxide films on metals, II, *Transactions of the faraday society* 35 (1940):472-483.
- [12] T. Grimley, B. Trapnell. The gas/oxide interface and the oxidation of metals. *Proceedings of the Royal Society of London A: Mathematical, Physical and Engineering Sciences*, vol. 234: The Royal Society, 1956. p.405-418.
- [13] P. Landsberg. On the logarithmic rate law in chemisorption and oxidation, *The Journal of Chemical Physics* 23 (1955):1079-1087.
- [14] G. Halsey Jr. The rate of adsorption on a nonuniform surface, *The Journal of Physical Chemistry* 55 (1951):21-26.
- [15] H.H. Uhlig. Initial oxidation rate of metals and the logarithmic equation, *Acta Metall Mater* 4 (1956):541-554.
- [16] V. Evans. *The corrosion and oxidation of metals (Second Supplementary Volume)*, 1976.
- [17] S. Sadique, A. Mollah, M. Islam, M. Ali, M. Megat, S. Basri. High-temperature oxidation behavior of iron–chromium–aluminum alloys, *Oxidation of Metals* 54 (2000):385-400.
- [18] V. Tolpygo, H. Grabke. Microstructural characterization and adherence of α -Al₂O₃ oxide scales on Fe-Cr-Al and Fe-Cr-Al-Y alloys, *Oxidation of Metals* 41 (1994):343-364.
- [19] F. Golightly, G. Wood, F. Stott. The early stages of development of α -Al₂O₃ scales on Fe-Cr-Al and Fe-Cr-Al-Y alloys at high temperature, *Oxidation of Metals* 14 (1980):217-234.

- [20] F. Stott, G. Wood, M. Hobby. A comparison of the oxidation behavior of Fe-Cr-Al, Ni-Cr-Al, and Co-Cr-Al alloys, *Oxidation of Metals* 3 (1971):103-113.
- [21] J.K. Bunn, R.L. Fang, M.R. Albing, A. Mehta, M.J. Kramer, M.F. Besser, J.R. Hattrick-Simpers. A high-throughput investigation of Fe-Cr-Al as a novel high-temperature coating for nuclear cladding materials, *Nanotechnology* 26 (2015):274003.
- [22] B. Jönsson, Q. Lu, D. Chandrasekaran, R. Berglund, F. Rave. Oxidation and creep limited lifetime of Kanthal APMT®, a dispersion strengthened FeCrAlMo alloy designed for strength and oxidation resistance at high temperatures, *Oxidation of metals* 79 (2013):29-39.
- [23] J. Smeggil, A. Shuskus. The oxidation behavior of some FeCrAlY, FeCrAl, and yttrium ion-implanted FeCrAl alloys compared and contrasted, *Journal of Vacuum Science & Technology A: Vacuum, Surfaces, and Films* 4 (1986):2577-2582.
- [24] J. Engkvist, S. Canovic, K. Hellström, A. Järnäs, J.-E. Svensson, L.-G. Johansson, M. Olsson, M. Halvarsson. Alumina scale formation on a powder metallurgical FeCrAl alloy (Kanthal APMT) at 900–1,100 C in dry O₂ and in O₂+ H₂O, *Oxidation of metals* 73 (2010):233-253.
- [25] G. Merceron, R. Molins, J.L. Strudel, I. Alliat, L. Menneron. Long term oxidation of FeCrAl ODS alloys at high temperature. *Materials science forum*, vol. 369: Trans Tech Publ, 2001. p.269-276.
- [26] D.J. Park, H.G. Kim, J.Y. Park, Y.I. Jung, J.H. Park, Y.H. Koo. A study of the oxidation of FeCrAl alloy in pressurized water and high-temperature steam environment, *Corrosion Science* 94 (2015):459-465.
- [27] R. Chegroune, E. Salhi, A. Crisci, Y. Wouters, A. Galerie. On the competitive growth of alpha and transient aluminas during the first stages of thermal oxidation of FeCrAl alloys at intermediate temperatures, *Oxidation of metals* 70 (2008):331.
- [28] C. Badini, F. Laurella. Oxidation of FeCrAl alloy: influence of temperature and atmosphere on scale growth rate and mechanism, *Surface and coatings technology* 135 (2001):291-298.
- [29] B.A. Pint, K.A. Terrani, Y. Yamamoto, L.L. Snead. Material selection for accident tolerant fuel cladding, *Metallurgical and Materials Transactions E* 2 (2015):190-196.
- [30] H.E. Kadiri, R. Molins, Y. Bienvenu, M.F. Horstemeyer. Abnormal high growth rates of metastable aluminas on FeCrAl alloys, *Oxidation of metals* 64 (2005):63-97.
- [31] S. Zhao, J. Zhang, D. Weng, X. Wu. A method to form well-adhered γ -Al₂O₃ layers on FeCrAl metallic supports, *Surface and Coatings Technology* 167 (2003):97-105.
- [32] H. Götlind, F. Liu, J.-E. Svensson, M. Halvarsson, L.-G. Johansson. The effect of water vapor on the initial stages of oxidation of the FeCrAl alloy Kanthal AF at 900 C, *Oxidation of metals* 67 (2007):251-266.
- [33] W. Quadakkers, D. Naumenko, E. Wessel, V. Kochubey, L. Singheiser. Growth rates of alumina scales on Fe-Cr-Al alloys, *Oxidation of metals* 61 (2004):17-37.
- [34] E.A. Gulbransen, K.F. Andrew. Oxidation Studies on the Iron-Chromium-Aluminum Heater Alloys, *Journal of the Electrochemical Society* 106 (1959):294-302.
- [35] R. Cuffe, H. Buscail, E. Caudron, F. Riffard, C. Issartel, S. El Messki. Effect of reactive element oxide coating on the high temperature oxidation behaviour of FeCrAl alloys, *Applied Surface Science* 229 (2004):233-241.
- [36] J. Jedlinski. The oxidation behaviour of FeCrAl ‘alumina forming’ alloys at high temperatures, *Solid State Ionics* 101 (1997):1033-1040.
- [37] W. Quadakkers, A. Elschner, W. Speier, H. Nickel. Composition and growth mechanisms of alumina scales on FeCrAl-based alloys determined by SNMS, *Applied Surface Science* 52 (1991):271-287.

- [38] C. Mennicke, E. Schumann, C. Ulrich, M. Rühle. The effect of yttrium and sulfur on the oxidation of FeCrAl. Materials science forum, vol. 251: Trans Tech Publ, 1997. p.389-396.
- [39] D. Naumenko, J. Le-Coze, E. Wessel, W. Fischer, W.J. Quadakkers. Effect of trace amounts of carbon and nitrogen on the high temperature oxidation resistance of high purity FeCrAl alloys, Materials Transactions 43 (2002):168-172.
- [40] J. Nychka, D. Clarke. Quantification of aluminum outward diffusion during oxidation of FeCrAl alloys, Oxidation of Metals 63 (2005):325-352.